Journal of Alloys and Metallurgical Systems 14 (2026) 100249

Contents lists available at ScienceDirect

Journal of Alloys and Metallurgical Systems

journal homepage: www.journals.elsevier.com/journal-of-alloys-and-metallurgical-systems

Additively manufactured carbide and nitride doped $Co_{22.2}Cr_{22.2}Ni_{22.2}Cu_{22.2}Nb_{11.2}$ high-entropy alloy for surface engineering application

Ayo Samuel Alabi [a,*], Abimbola Patricia Idowu Popoola [a], Olawale Mohammed Popoola [b], Ntombi Ruth Mathe [a,c]

[a] Chemical, Metallurgical and Materials Engineering, Faculty of Engineering and Built Environment, Tshwane University of Technology, P.M.B. X680, Pretoria, South Africa
[b] Centre for Energy and Electric Power, Electrical Engineering, Faculty of Engineering and Built Environment, Tshwane University of Technology, P.M.B. X680, Pretoria, South Africa
[c] Photonics Centre, Council for Scientific and Industrial Research, Pretoria, South Africa

ARTICLE INFO

Keywords:
Surface engineering
HEA-based composites
Microhardness
Tribological properties
Corrosion resistance

ABSTRACT

Metal-matrix composites have gained wide recognition owing to their superior tailorability, which surpasses that of traditional alloys. The development of multicomponent metal-based high-entropy alloy (HEA) systems has increased the potential for fabricating tunable composites for surface engineering applications. It has been established that the intrinsic properties of the composites are determined by the phases present in their base alloys, reinforcement types, and volumes. Herein, 5 wt% of vanadium carbide, titanium nitride, and a combination of both ceramics were added to $Co_{22.2}Cr_{22.2}Ni_{22.2}Cu_{22.2}Nb_{11.2}$ HEA and fabricated via directed-energy deposition. The investigation highlights the first-time use of both ceramics and their synergistic utilisation as hybrid reinforcement in the directed-energy-deposited HEA. The candidate with the best hardness, tribological properties, and corrosion resistance was identified after various characterisations. It was found that the composite reinforced with a combination of both ceramics had the best microhardness value of 736 ± 30.79 HV. The titanium nitride-reinforced composite exhibited the highest wear resistance with 6.69×10^{-6} mm^3 /Nm at 20 N applied load. However, the synergy of both reinforcements offers enhanced lubricity, resulting in the lowest coefficient of friction of 0.071. A worn track analysis revealed that the samples were characterised by a transition from severe adhesive wear to cold-welded tribo-layer formation. The unreinforced HEA demonstrated the highest corrosion resistance with 567.79 Ω polarisation resistance and a corrosion rate of 0.6909 mm/year. It was concluded that the developed HEA and its composites are promising candidates for surface engineering application.

Introduction

The CoCrNi medium-entropy alloy exhibits promising mechanical properties that are comparable to those of the best cryogenic steels. The alloy's superior properties to those of other low-, medium-, and HEA of the Cantor alloy family have made it gain considerable research attention as a promising material for structural application. Many attempts to enhance its overall mechanical properties using alloying strengthening mechanisms have been reported [1–3]. The attempts have resulted in the emergence of many other CoCrNi-based medium- and high-entropy alloys (MHEAs) and the realisation that this class of alloy is suitable for surface engineering applications. The composition of the alloy has been tuned to achieve excellent tribological properties, outstanding corrosion resistance, and high oxidative and radiation stabilities [2,4,5].

Surface science and engineering have made significant progress in customising the surface properties of diverse materials for specific applications. It encompasses several processes for modifying a substrate through the deposition of overlayers to tune the mechanical, thermal, chemical, optical, and electrical properties [6]. Lattice distortion has been reported to be a major factor that influences the properties of

* Corresponding author.
E-mail addresses: 222896401@tut4life.ac.za (A.S. Alabi), popoolaapi@tut.ac.za (A.P.I. Popoola), popoolao@tut.ac.za (O.M. Popoola), nmathe@csir.co.za (N.R. Mathe).

https://doi.org/10.1016/j.jalmes.2026.100249
Received 9 March 2026; Received in revised form 26 April 2026; Accepted 7 May 2026
Available online 8 May 2026

MHEAs. The addition of large atomic radii or interstitial atoms can induce severe lattice distortion that often greatly impacts the structural and functional properties of MHEAs, making them better candidates for surface engineering applications than conventional alloys [5]. Moravcik et al. [7] achieved interstitial solid solution and precipitation strengthening of a CoCrNi MEA by doping it with carbon, which led to the enhancement of the alloy's mechanical properties, achieving an ultimate tensile strength of 1180 MPa and more than 60% elongation at 0.5 at% carbon doping. Jodi and Park [8] observed the transformation from single FCC to dual Cu-rich and Cu-lean FCC phases upon the addition of copper (Cu) to the CoCrNi MEA. The phase separation resulted in an atomic-size misfit that affected atomic interaction in the alloy system; hence, the Cu-rich phase exhibited lower microhardness than its Cu-lean counterpart. Ren, et al. [9] reported that the low-hardness Cu-rich phase in the CoCrNiCux alloy system formed well-distributed nanoprecipitates after thermal annealing. The precipitates were found to be beneficial in preventing dry sliding wear owing to their deformation into a tribolayer that led to subsurface hardening and enhanced wear resistance. Lu et al. [10] studied the effect of niobium (Nb) addition on the structure and mechanical properties of CrCoNi MEA. The addition resulted in the formation of an ordered Nb-rich Laves phase, which balanced the strength and ductility of the alloy. Thereby reducing the fracture strain from 40.2% to 11.3% and enhancing the compressive yield strength from 748 to 2080 MPa. The hardness value of the alloy was also improved from 193 HV for CoCrNi to 700 HV with a 0.5 Nb addition. Ding et al. [11] added aluminium (Al) to CoCrNi MEA and achieved a dual phase separation that improved the alloy's oxidation resistance owing to the formation of spinel oxides. The hardness value, yield and compressive strengths also increased to 646 HV, 2083 and 2498 MPa, respectively. Along the same line, Wu, et al. [12] also investigated the impact of Nb variation on the phase evolution, microstructural transformation, corrosion, and wear resistance of CrCoNiFeNbx. The changes in phase and microstructure due to Nb variation resulted in a coating with a hardness value of about 530 HV, a 44% improvement in wear resistance, and a superior corrosion resistance compared to that of the stainless-steel substrate.

Riva et al. [13] remarked that "given the fact that attractive properties of metal matrix composites (MMCs) are achieved via composition tuning, it is surprising that MHEA-based composites have not been widely investigated. Since 2018, substantial advancements have been made by researchers in the application of MHEA matrices within MMCs. Various ceramics have been employed as reinforcements in numerous MHEAs due to their role in enhancing properties [14–16]. The incorporation of ceramic particles has proved effective in improving both mechanical and tribological properties of MHEAs. This improvement happens because ceramic particles pin the grain boundaries, which stops the grains from growing. This makes the grains stronger and more refined. Additionally, dispersed ceramic particles can act as durable reinforcing phases that obstruct dislocation slip and diminish plastic deformation [17]. Wang et al. [18] introduced varying amounts of tungsten carbide (WC) into FeCoCrNiMn HEA-based coatings, fabricating the coatings via the plasma surfacing method. Investigations into the microstructural evolution and the mechanical and fracture properties revealed that the inclusion of WC altered the coatings' texture from coarse to fine grains. This transformation resulted in improvements in hardness, strain, yield strength, and tensile strength, increasing to 514.9 ± 48.1 HV, 2.7%, 457 MPa, and 517 MPa, respectively, from initial values of 198.8 ± 15.6 HV, 53.7%, 225 MPa, and 478 MPa, at a 40 wt% addition of WC. Liang et al. [19] selected titanium nitride (TiN) as a reinforcement for AlCoCrCuNiTi HEA, highlighting its isotropy, excellent chemical stability, high hardness, and modulus as properties that could enhance the exceptional ductility of the base HEA. The coherent interfacial interaction between the ceramic and the HEA was identified as an additional advantage. Researchers also investigated the hardness and wear properties of composite coatings on TC4 alloy, discovering that the addition of TiN increased the hardness from 628 HV to 737 HV, which signifies a notable increase from the 320 HV hardness of the TC4 alloy base metal. This enhancement in hardness was also associated with improved wear resistance of the coatings. Similarly, Han et al. [17] examined the impact of double ceramic reinforcement on the wear properties of FeCoCrNiAl HEA coating. The combined addition of niobium carbide (NbC) and TiN led to a synergistic effect, resulting in grain refinement that enhanced the microhardness of the coating by 55.08% and significantly reduced the wear rate by 88.38% when compared to 17–4PH stainless steel. The authors noted that NbC had a milder effect on grain refinement in the base HEA alloy in isolation compared to the synergy observed with both NbC and TiN. Yu et al. [20] developed TiC- and Mo-enhanced AlCoCrFeNiMox(TiC)x-2 HEA coatings, with x values of 0.5, 1, 1.5, and 2. They studied the phase evolution, microstructure, hardness, corrosion resistance, and high-temperature oxidation resistance of the alloys. The optimal oxidation and corrosion resistance was found at x = 1, achieving approximately 12% oxidative stability and 83% corrosion resistance compared to the other coatings.

Table 1
Chemical Composition of the $Co_{22.2}Cr_{22.2}Ni_{22.2}Cu_{22.2}Nb_{11.2}$ HEA.

Element	Cobalt	Chromium	Nickel	Copper	Niobium
Atomic %	22.2	22.2	22.2	22.2	11.2

The performance of composite-based coatings derived from multi-principal element MHEAs for surface engineering applications fundamentally depends on the phases present in the base MHEAs, as well as the type and volume of the reinforcing particles added [21]. According to the reports of the authors cited thus far, it has been established that the properties of MHEAs and their composites can be tailored through compositional or constitutional variations. In this study, a directed-energy deposited $Co_{22.2}Cr_{22.2}Ni_{22.2}Cu_{22.2}Nb_{11.2}$ HEA was reinforced with 5 wt% of VC, TiN, and a combination of both ceramics, specifically 2.5 wt% VC and 2.5 wt% TiN. This represents the pioneering first-time use of VC, TiN, and the synergies between VC and TiN in a $Co_{22.2}Cr_{22.2}Ni_{22.2}Cu_{22.2}Nb_{11.2}$ HEA via additive manufacturing. Directed energy deposition additive manufacturing was selected due to its rapid deposition rate for coatings on metal substrates, its capacity to form superior metallurgical bonding between the coating and substrate while minimising defects, its versatility in using multi-component powder feedstock, and its suitability for repairing worn metallic surfaces [22]. The phase and microstructural evolution and hardness values, as well as the wear and corrosion resistances, of the composites were evaluated and compared to those of the base HEA. The candidates that demonstrated superior performance across various tests were identified for potential surface engineering applications, including cladding and surface alloying.

Experiment and characterisation

Materials

All powders, apart from Nb, VC, and TiN, used in the fabrication of the $Co_{22.2}Cr_{22.2}Ni_{22.2}Cu_{22.2}Nb_{11.2}$ HEA and its composites were supplied by Weartech, South Africa. These powders have a purity of 99.9% and a particle size of 90 + 45 μm. Nb, VC, and TiN, which have mesh sizes of 325, were supplied by Zhengzhou Alfa Chemical Company, Singapore.

Table 2
The Composition of the $Co_{22.2}Cr_{22.2}Ni_{22.2}Cu_{22.2}Nb_{11.2}$ HEA and its composites.

Based and Reinforcements	**Composites composition (wt%)**		
	HEA-VC	**HEA-TiN**	**HEA-VC-TiN**
HEA	95	95	95
VC	5	-	2.5
TiN	-	5	2.5

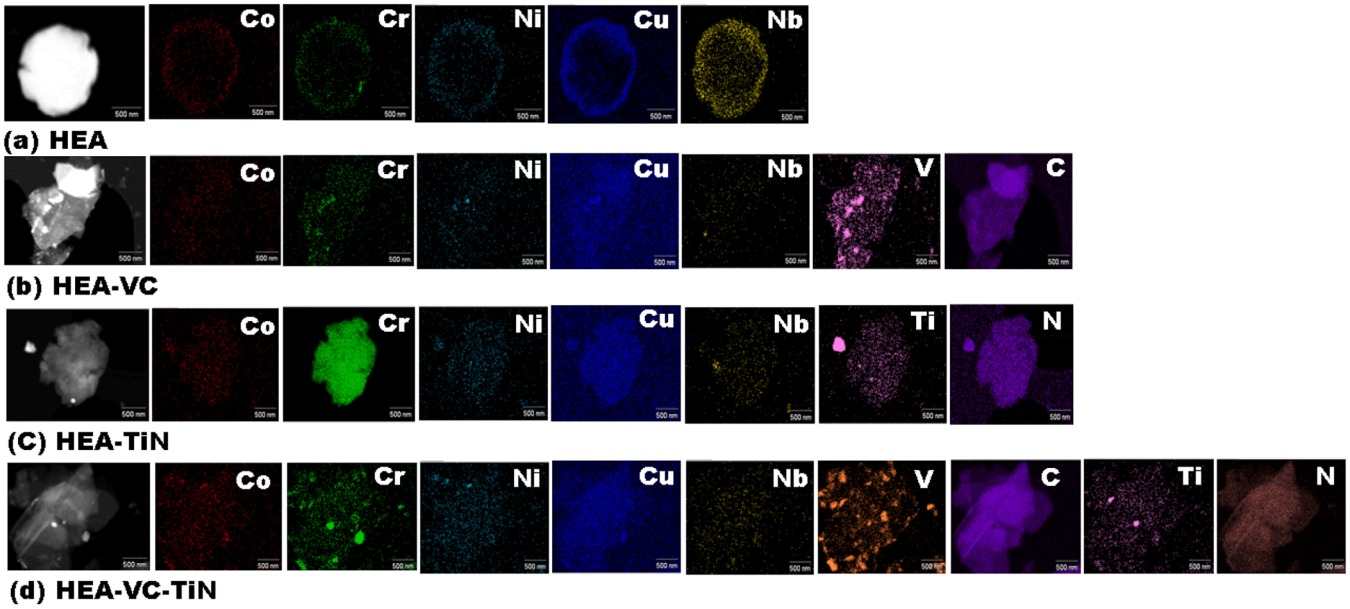

Fig. 1. Elemental mapping of mixed powders.

Fabrication of the HEA and its composites

The $Co_{22.2}Cr_{22.2}Ni_{22.2}Cu_{22.2}Nb_{11.2}$ HEA and its composites were fabricated using directed-energy deposition additive manufacturing with an IGP fibre laser. The chemical compositions of the HEA and its composites are detailed in Tables 1 and 2, respectively. Rectangular cuboid samples, measuring 30 × 10 × 5 mm, were deposited on Ti-6Al-4V baseplates. The baseplates were preheated to 400°C on a preheating platform, and the samples were fabricated at this temperature. Following fabrication, the samples were allowed to cool slowly on the preheating stage to mitigate crack sensitivity associated with rapid cooling.

The samples were produced with a constant beam diameter of 2.0 mm, a carrier gas flow rate of 2.0 l/min, and a central purge gas flow rate of 20 l/min. The directed-energy deposition parameters included a laser power of 1200 watts, a scanning speed of 1.2 m/min, and a powder flow rate of 0.24 g/min, all at a 50% track overlap. The samples were created using preprogrammed CAD files. The parameters were optimised through parametric trials to achieve a densification of over 95% (according to Archimedes' principle) and to minimise porosity, thus ensuring a balance between melt pool stability, uniform reinforcement distribution, and the retention of phases within the HEA matrix.

Characterisation method

The micrographs of the mixed powders and the directed-energy-deposited HEA and its composites were obtained using a JEOL-JSM-6010 PLUS/LAM scanning electron microscope as well as a JEM-2100 transmission electron microscope (TEM). All samples that were additively manufactured were sectioned and mounted for metallurgical preparation using an automatic mounting press, facilitating handling during the preparation process. A Struers TegraForce-5 auto/manual polisher was employed to grind and polish the samples. Subsequently, the samples were etched with a marble reagent prior to metallographic examination. The X-ray diffraction (XRD) patterns of all samples were determined using PANalytical Empyrean X-ray diffraction equipment, operating at 20 mA and 40 kV and using a Cu-Kα source. The XRD peaks were characterised with the aid of X'pert HighScore Plus software, which is equipped with the ICDD Match 139 database. The crystallite sizes, crystal lattice microstrains, and dislocation densities of the HEA and its composites were analysed through Scherer's analysis of the X-ray diffraction data, utilising Eqs. 1–3.

$$Crystallite\ size\ (D) = \frac{0.89\lambda}{\beta\cos\theta} \quad (1)$$

$$Micro-strain\ (\varepsilon) = \frac{\beta}{4\tan\theta} \quad (2)$$

$$Dislocation\ density\ (\delta) = \frac{1}{D^2} \quad (3)$$

Where λ = The wavelength of the X-ray used
β = The full width at half maximum
θ = The peak position

The Archimedes principle was employed to determine the experimental densities of the HEA and its composites using the Ohaus Explorer densometer according to the ASTM B962 standard. An average of 3 readings was recorded for each sample. The theoretical densities of samples were also calculated using the classical rule of mixture. Thereafter, the relative densities of samples were then calculated as the ratio of measured to calculated densities. The relative densities of the samples denote their percentage of densification; hence, their deficit from 100% was recorded as the percentage porosities of the samples.

The microhardness of the composites was determined using a Zwick/Roell Indentec (ZHVμ) Vickers hardness machine. The test was conducted under a force load of 300 g, a dwell time of 10 s, and a spacing of 100 μm as per the ASTM E384 standard. An average of ten indentations was recorded for each sample.

The wear rate and coefficient of friction of the HEA and its composites were determined at room temperature using a TRB3 Anton Paar tribometer attached to an S128 Surtronic profilometer in a ball-on-flat rotating configuration. A 6 mm steel ball was used as the sliding counterbody. The tests were conducted according to ASTM G99 under varying loads of 10, 15 and 20 N and a sliding cycle of 6000 at a radius of 0.3 mm. The worn track analysis of the samples was performed using an attached Surtronic profilometer.

Potentiodynamic polarisation tests per ASTM G57–97 were performed using a three-electrode setup on an Autolab electrochemical workstation PGSTAT 302 potentiostat/galvanostat. The evaluation started with an open-circuit potential (OCP) test for 1 h at ambient temperature. The HEA and its composites were used as the working electrode with a 1 cm^2 surface of the samples exposed to the 0.5 M H_2SO_4

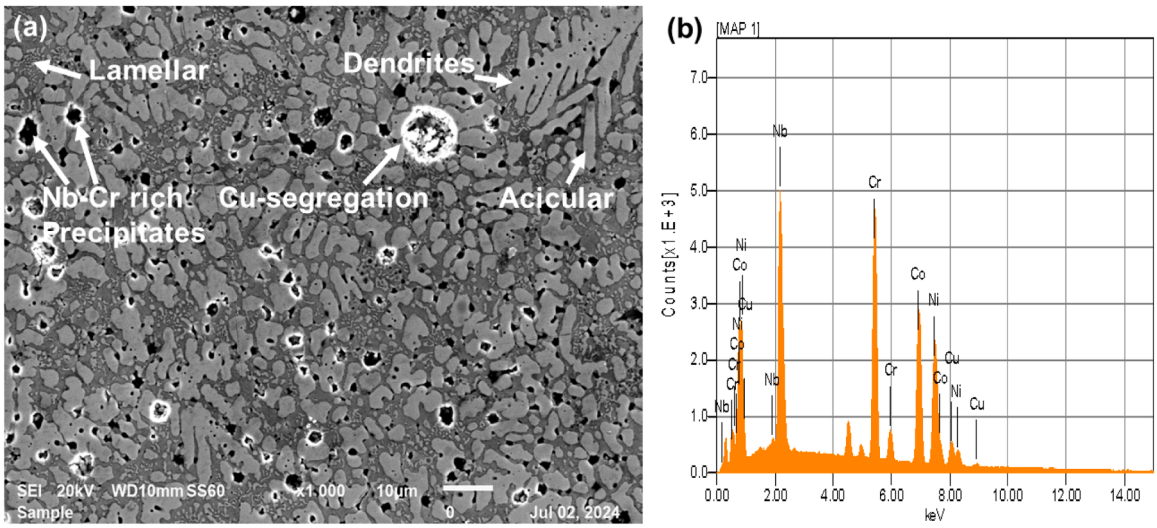

Fig. 2. SEM/EDS images of the HEA.

electrolyte to simulate an acidic industrial environment and enable the evaluation of the ability of the composites to form passive films owing to the presence of niobium and chromium in the HEA matrix. An Ag/AgCl electrode and a platinum rod were used as the reference and counter electrodes, respectively. Prior to the corrosion tests, the samples were washed with distilled water, degreased with acetone, and dried in a desiccator. Thereafter, the samples were cold mounted in an epoxy resin. The mounted samples were polished, cleaned, degreased again, and washed with ethanol before the corrosion test.

Results and discussion

Elemental mapping of mixed powders

Fig. 1a–d present TEM/EDS images illustrating the elemental mapping of the $Co_{22.2}Cr_{22.2}Ni_{22.2}Cu_{22.2}Nb_{11.2}$ HEA and its ceramic-doped powders prior to fabrication. Fig. 1a indicates that the constituent elements were well dispersed, thereby confirming the even distribution of the powders. Fig. 1b–d depict various ceramics that have been doped with the HEA powder, with the mapping indicating a uniform distribution of ceramics within the HEA matrix. The distinct distribution of VC, TiN, and the combination of both ceramics further validates that the HEA powder was effectively doped with different ceramics before the additive manufacturing process.

Microstructural characterisation of the HEA and its composites

Fig. 2a and b illustrate the morphology and EDS elemental intensity of the HEA. The alloy features a well-distributed Nb-Cr-rich network, characterised by dendritic, lamellar, acicular, and coarse precipitate solidification structures. The precipitates display a ring-like morphology, with a dark core and bright peripheral fringes, potentially due to topographic edge effects observed in scanning electron microscopy (SEM). Wang et al. [23] and Hong et al. [24] have reported that incorporating Nb into CoCrNi-based alloys leads to the formation of an Nb-Cr-rich network. Additionally, the alloy exhibits significant elemental copper (Cu) segregation, indicative of preferential macro-segregation of Cu clusters, attributed to its immiscibility with the melted bulk of the HEA constituent elements. The array of segregated Cu clusters presents a bright contrast within the HEA matrix. Pan et al. [25] noted the segregation of solute Cu in a CoCrNiCux alloy system, while Cai et al. [26] documented a similar Cu segregation in a directed-energy deposited FeCoCrNiCux HEA.

The addition of VC, TiN, and the combination of both ceramics to the HEA resulted in notable morphological changes, as demonstrated in the SEM/EDS images shown in Fig. 3a–f. The EDS peaks confirmed the presence of the elemental constituents within the composites. Morphological alterations were observed across all composites due to the dispersion effects of the various ceramics incorporated into the HEA matrix. Adding these ceramics helps to refine the grains and stop dendritic growth during solidification. This is because the ceramic particles act as heterogeneous nucleation sites, which speeds up the nucleation rate of the solid phase from the melt pool [27,28]. This process leads to more refined and compact structures while suppressing solidification features such as lamellar, acicular, and coarse precipitates within the HEA matrix.

Phase identification of the HEA and its composites

The XRD patterns of the HEA and its composites are presented in Fig. 4. The diffractogram indicates the presence of both CoCrNi (FCC1) and $Cu_{81}Ni_{19}$ (FCC2) phases, alongside Cr (Co,Ni)Nb-type HCP Laves phases within the HEA. Additionally, the diffraction peaks demonstrate the emergence of new peaks following the incorporation of various ceramics. Notably, the addition of VC resulted in a narrowing of the primary diffraction peak of the HEA, whereas the introduction of TiN led to a slight broadening of the same peak. This observed narrowing and broadening of the characteristic peak may be attributed to the doping effects of the different ceramics on the HEA. Zhang et al. [29] observed a carbide-induced lattice distortion in a TiC-reinforced $Fe_2CoNiCrAl$ composite, and Chen et al. [30] reported a similar phenomenon related to the reinforcement of CoCrFeMnNi with TiC.

Additionally, a noticeable increase in the peak intensity in the HEA characteristic peak was observed when TiN was added, which is attributable to the grain boundary pinning by the dispersed ceramic particles. Li et al. [31] also observed a peak broadening in CoCrFeMnNi reinforced with TiN nanoprecipitates; the authors attributed the observation to induced dislocation pinning in the lattice crystal due to the grain refinement effect of the TiN. Along the same line, Table 3 showed a decrease in crystallite size from 10.35 to 4.50 nm and increased severity in dislocation density (0.012–2.500 nm^{-2}) and micro-strain (0.0017–0.0055%) of the TiN-reinforced HEA owing to the ceramic dispersion effect. Similarly, Jin, et al. [32] noticed an increase in peak intensity after adding TiN to AlCoCrFeNi. Moreover, the XRD peaks of the HEA and all its composites indicated multi-phase systems with distinct peaks and phase overlapping for CoCrNi-rich FCC1, Cu-Ni-rich FCC2, Cr (Co, Ni) Nb-type Laves phases, VC, and TiN reinforcements observed in the diffraction patterns, suggesting multiple strengthening

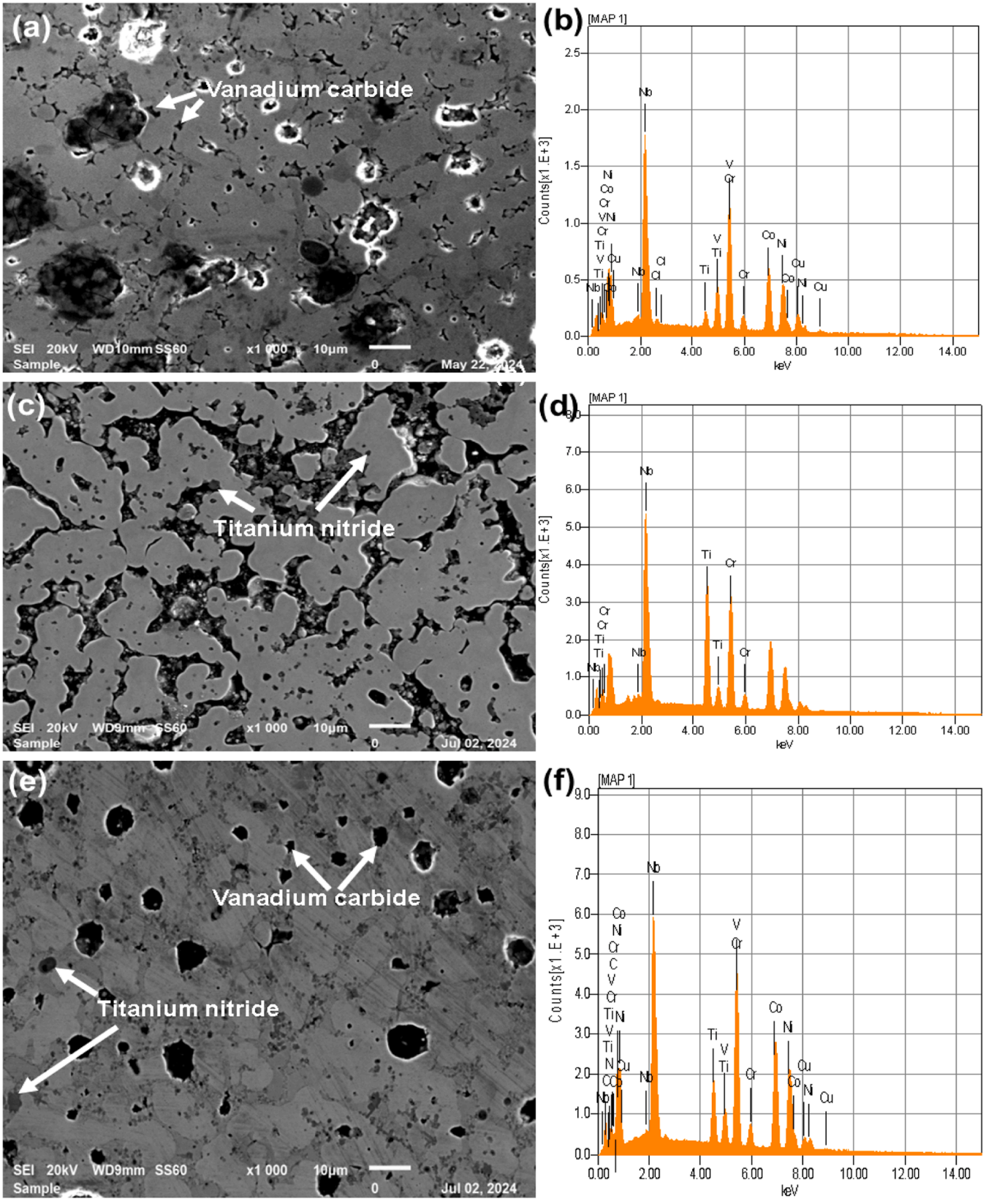

Fig. 3. SEM/EDS images of the (a) HEA-5wt%VC (c) HEA-5wt%TiN (e) HEA-2.5 wt%VC-2.5 wt%TiN.

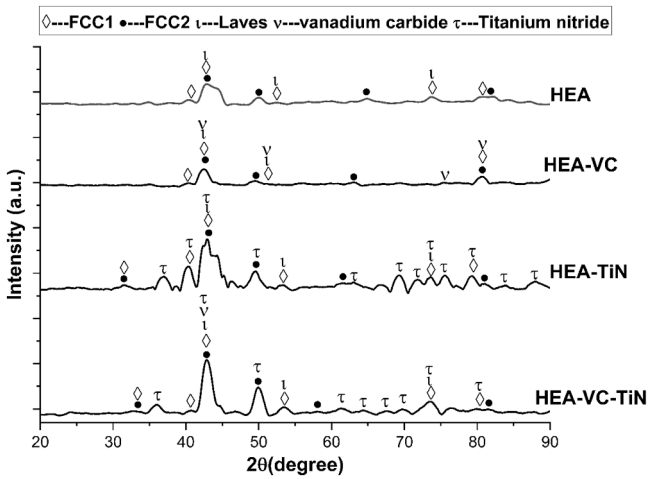

Fig. 4. X-ray diffraction patterns of HEA and its composites.

Table 3
Crystallite size, lattice strain and dislocation density of the HEA and its composites.

Samples	Crystallite size (nm)	Micro-strain (%)	Dislocation density (nm^{-2})
HEA	10.35	0.0017	0.012
HEA-5%VC	7.64	0.0030	0.030
HEA-5%TiN	4.50	0.0055	2.500
HEA-2.5%VC-2.5%TiN	0.07	0.0073	122.970

mechanisms in the composites. The observation agrees with the multi-structured microstructures presented in Figs. 2 and 3.

The diffraction pattern of the HEA-VC-TiN composite reveals an overlap between the diffraction peaks of the HEA-VC and HEA-TiN composites. The observed crystallite size is 0.07 nm, with a dislocation density of 122.970 nm^{-2} and a micro-strain of 0.0073%. These findings suggest that the combination of both ceramics significantly enhanced the composite's grain refinement. However, this process resulted in a geometric increase in dislocation density from 0.012 nm^{-2} for the HEA to 122.970 nm^{-2} for the HEA-VC-TiN composite, thereby inducing greater micro-strain of 0.0073% in the composite's lattice.

Fig. 5 illustrates the electron backscattered diffraction (EBSD) features of the HEA and its VC- and TiN-reinforced composites. The colours present in the HEA image confirmed that the alloy formed polycrystalline structures with different crystallographic orientations. The added ceramic reinforcements are also well dispersed in the matrix of the HEA.

The phase maps reveal the microstructural evolution upon the incorporation of VC and TiN reinforcements into the HEA matrix. The base alloy is dominated by CoCrNb, CoCrNi, $Cu_{81}Ni_{19}$ and $CrNb_2$ phases. The addition of VC resulted in a refined grain structure compared to the unreinforced alloy. The VC particles, identified by their distinct crystallographic signature in EBSD, act as nucleation sites and exert a pinning effect on grain boundaries during solidification. The phenomenon suppressed grain growth and promoted a more equiaxed morphology. The dispersion of carbides within the HEA matrix is beneficial for enhancing hardness and yield strength via the Orowan strengthening mechanism [33]. On the other hand, the addition of TiN to the matrix contributed to a high density of dislocation accumulation at the matrix-reinforcement interface. The black spots observed in the phase maps represent non-indexing or zero solutions, demonstrating that the electron beam could not collect reliable signals for indexing and crystal structure identification, often due to lattice distortions or the presence of pores or cracks. Fig. 5a reveals the occurrence of the black

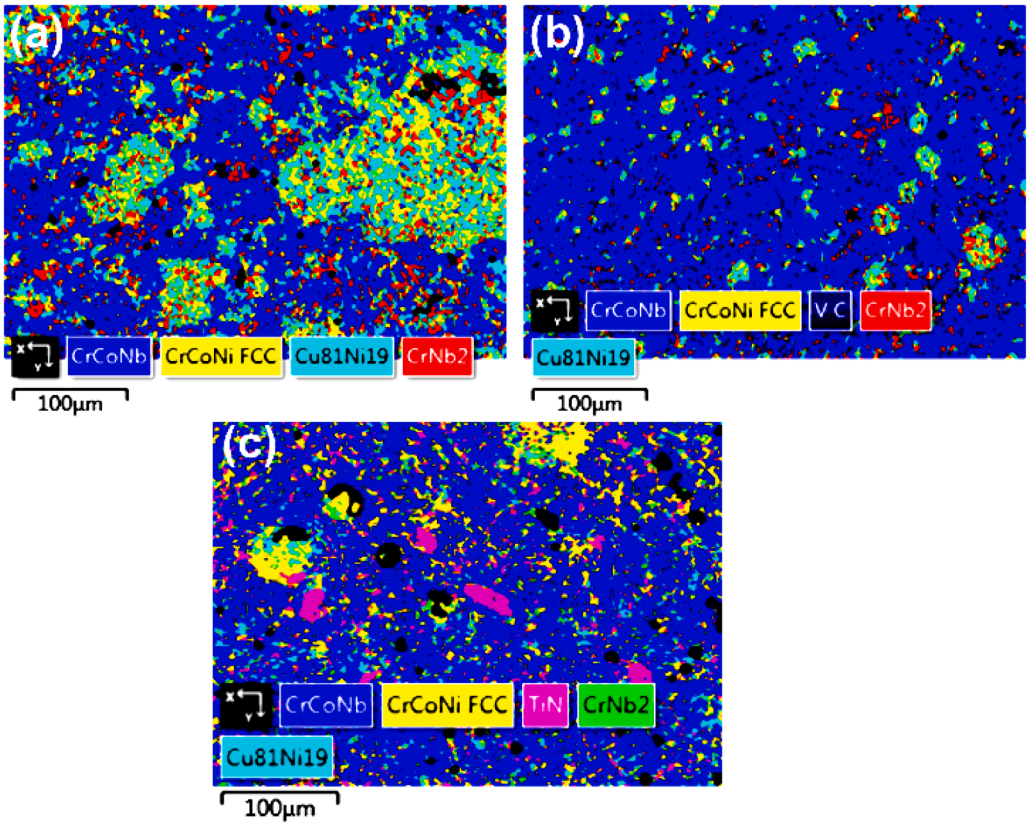

Fig. 5. EBSD phase mapping of (a) HEA (b) HEA-VC and (c) HEA-TiN.

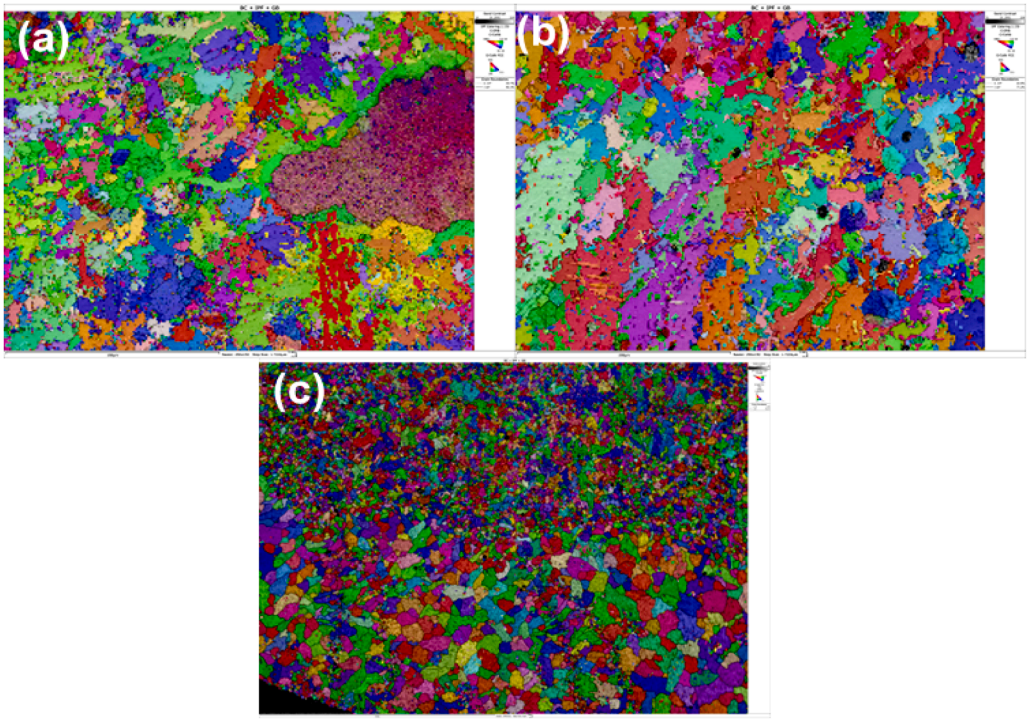

Fig. 6. Grain distributions of (a) the HEA (b) HEA-VC and (c) HEA-TiN.

spots at the grain boundaries and constituent phases' interfaces, suggesting that lattice mismatch and internal strains are highest at such spots within the HEA matrix. The black spots increase around carbide particles in the VC-reinforced HEA, as shown in Fig. 5b, probably due to the mismatch in thermal expansion coefficients between the carbide and the matrix during cooling, hence the increase in micro-strain presented in Table 3.

The grain analysis revealed a random orientation of grain distribution within the particles, as illustrated in the orientation maps in Fig. 6. The evolution of the maps presented in Figs. 6a and 6b indicates a refined grain structure due to the addition of VC to the HEA matrix. The significant reduction in average grain size shown in Fig. 6c, in comparison to the matrix, suggests that the added TiN particles serve as nucleation sites, while the VC particles contribute to a grain boundary pinning effect [34,35]. Fig. 5c demonstrates that the TiN-reinforced HEA exhibits larger black spots surrounding large particles or agglomerations of TiN, which indicates strain accumulation. In contrast, regions with a homogeneous distribution of TiN show a reduction in black spots, attributed to a decrease in large-scale lattice distortions.

The map in Fig. 6c demonstrates a more heterogeneous microstructure with a high density of low-angle grain boundaries. The colour gradients within individual grains suggest the accumulation of geometrically necessary dislocations. The localised lattice distortions are characteristics of HEAs and are further intensified by the stress fields

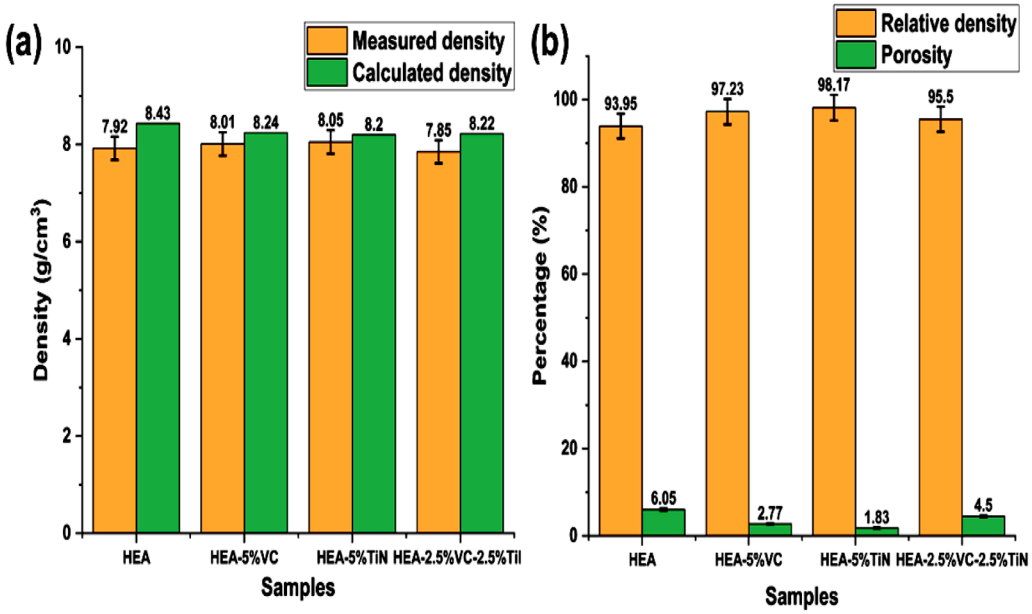

Fig. 7. (a) Densities (b) Relative densities and porosity of the HEA and its composites.

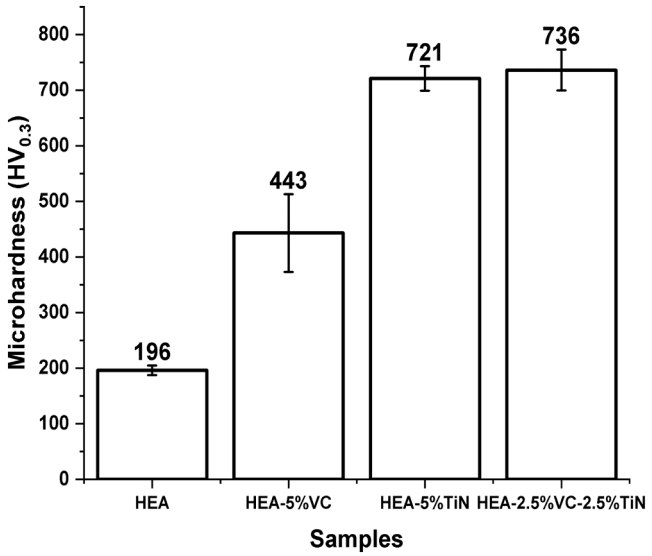

Fig. 8. Microhardness of the HEA and its composites.

generated around hard ceramic reinforcements. Such high-density boundary networks are indicative of Hall-Petch strengthening and contribute to superior hardness and wear resistance observed in HEA-based composites [36]. Overall, the addition of VC and TiN to the HEA matrix served the dual role of grain boundary pinning and acting as nucleation sites. Han, et al. [17] reported a beneficial synergistic effect of the combination of NbC and TiN on an HEA that resulted in grain refinement and enhancement of the composite's hardness and tribological properties.

Density and porosity of the HEA and its composites

Optimised directed-energy deposition parameters enhance densification and minimise porosity in high-entropy alloys (HEAs) and their composites, thereby promoting structural integrity and enhancing properties [34,35]. Fig. 7a and b illustrate the measured and calculated densities, relative densities, and porosities of the HEA and its composites. The samples exhibited lower measured densities compared to their calculated values, indicating incomplete densification, as evidenced by the relative densities. Contrary to expectations, the ceramic-reinforced composites demonstrated higher densities than the unreinforced HEA. This trend may be attributed to the greater levels of porosity present in the HEA compared to its composites. The porosity contributions were specifically measured at 6.05%, 2.77%, 1.83%, and 4.50% for the HEA, VC, TiN, and VC-TiN reinforced composites, respectively. The relative densities indicate that the incorporation of various ceramics into the HEA resulted in improved densification of the composites.

The TiN-doped composite achieved optimal densification with a relative density of 98.17%, representing a significant enhancement over the 93.95% relative density of the HEA matrix. The improved densification in the composites is clearly linked to the grain refinement illustrated in Fig. 6, which leads to a more compact structure. Wang et al. [36] reported a relative density of 99.72% in additively manufactured CoCrFeMnNi HEA reinforced with 5% TiB_2.

Microhardness and wear characteristics of the HEA and its composites

The graph presented in Fig. 8 illustrates the microhardness values of the HEA and its composites.

The hardness value of the HEA was measured at 196 ± 8.55 HV, while the VC-reinforced composite demonstrated a significant enhancement, recording a hardness value of 443 ± 69.64 HV, more than double that of the HEA. This improvement in hardness can be attributed to the expected synergistic effects of solid solution and dispersion strengthening provided by the HEA and VC reinforcement. Chen et al. [37] identified combined strengthening mechanisms in the TiC-reinforced FeCoCrNiCu HEA. In contrast, the composite reinforced with TiN achieved a notable hardness of 721 ± 22.28 HV, attributed to multiple strengthening mechanisms, including the Hall-Petch effect, as illustrated in Fig. 6c. Furthermore, Liang et al. [19] reported a TiN-induced dispersion strengthening effect in the AlCoCrCuNiTi HEA, which complemented other strengthening mechanisms, such as solid solution and intermetallic phase strengthening.

An optimum hardness value of 736 ± 30.79 HV was attained in the composite reinforced with both VC and TiN, which can be attributed to the synergistic effects of these ceramics. The reinforcements fulfil a dual role as heterogeneous nucleation sites and as agents for grain boundary pinning. This illustrates the synergistic advantage of achieving a higher hardness value compared to instances where the ceramics are employed as reinforcements individually.

Overall, the dispersion of both ceramic particles within the matrix of the HEA significantly enhanced hardness through mechanisms of solution and dispersion strengthening. Furthermore, VC contributed to a finer dispersion (Fig. 5b), which effectively pinned dislocation propagation. This is evidenced by the increase in dislocation density from

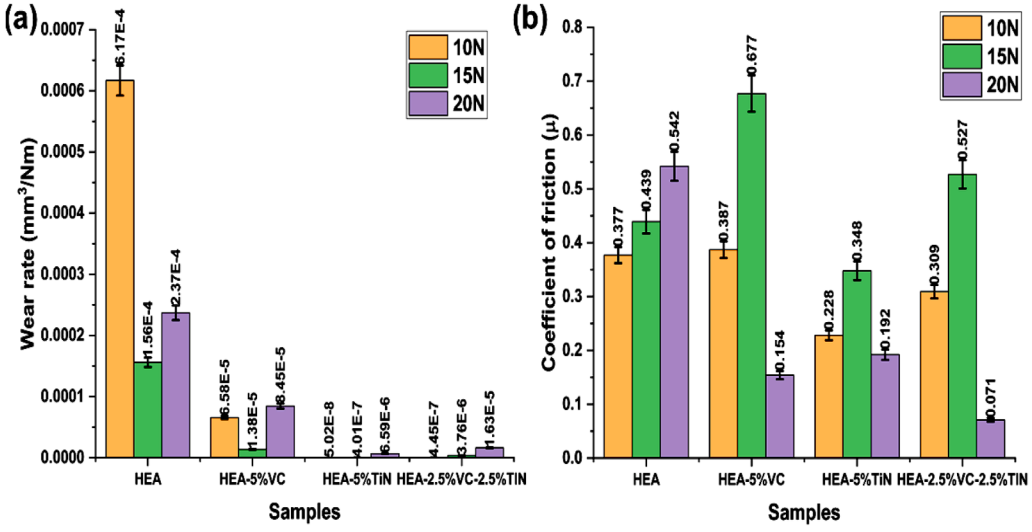

Fig. 9. (a) Wear rate and (b) Coefficient of friction of the HEA and its composites.

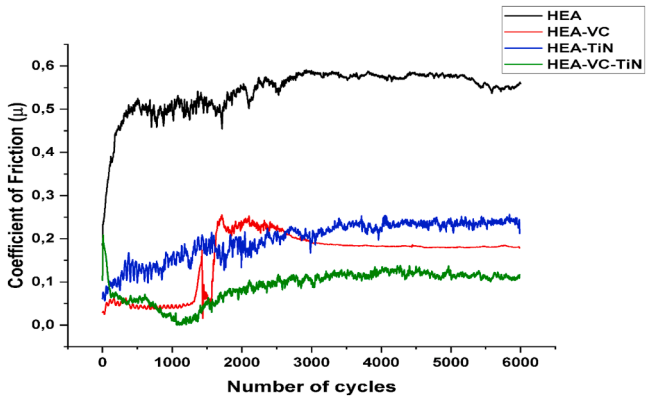

Fig. 10. Coefficient of friction vs number of cycle profile.

0.012 nm^{-1} for the HEA matrix to 0.030 nm^{-1} in the VC-reinforced composite, as detailed in Table 3. In contrast, the coarser dispersion of TiN particles, as shown in Fig. 5c, elevated the hardness value from 196 ± 8.55 HV to 721 ± 22.28 HV and hindered dislocation motion, resulting in an increase in dislocation density from 0.012 nm^{-1} for the HEA matrix to 2.5 nm^{-1} for the TiN-reinforced composite (Table 3). The combination of VC and TiN synergistically improved grain boundary pinning and obstructed dislocation motion through the creation of multi-scale barriers, leading to a further increase in dislocation density to 122.970 nm^{-1} .

The wear rates (Fig. 9a) of the HEA and its composites, tested under applied loads of 10, 15, and 20 N, indicated that all the composites displayed superior wear resistance compared to the HEA.

This finding correlates with the microhardness results and agrees with the Archard law, which states that wear rate is directly proportional to the applied normal load and sliding distance and inversely proportional to the hardness value of a material [38]. An increase in wear resistance was observed for the HEA as the applied load increased, which may possibly be due to the formation of a plastically deformed ductile CoCrNI and Cu-rich phase that formed compacted tribolayers when reinforced by the hard Laves phase and hindered further frictionally induced surface damage. Ren et al. [9] had earlier reported the formation of tribolayers by segregated Cu-rich nanoprecipitates in the CoCrNiCux alloy system, while Lu et al. [10] mentioned that the addition of Nb resulted in the formation of a hard Laves phase in the CoCrNiNbx MEA. Moreover, a different trend was observed when various ceramics were added to the HEA. The incorporation of the ceramics generally improved the wear resistances of the composites. The improvement may be explained via the Orowan mechanism, where non-shearable dispersed ceramic particles force dislocation pile-up to bow around them. This process formed Orowan dislocation loops that increased strain hardening and resisted plastic deformation during sliding [39,40]. The VC addition minimised wear via Orowan looping and carbide-wear debris compaction, while the TiN reinforcement reduced abrasive ploughing owing to its high hardness, wear resistance and excellent lubricating properties that greatly reduced direct contact points during sliding. The synergy of both ceramics enabled the formation of a tribo-film from compacted wear debris that acted as a low-shear tribo-layer, which reduced friction coefficients and transitioned wear from adhesive form to non-direct contact protective layer mode. Conversely, the coefficient of friction (COF) of the HEA increased from 0.377 to 0.439 and 0.542 at applied loads of 10, 15 and 20 N, as shown in Fig. 9b, indicating an increase in friction between the contacting surfaces as the sliding load increased owing to the higher frictional contact force. However, a decrease in the COF was observed in the composites as the applied load increased, which may be due to the wear debris-reinforcement's forming protective tribo-layer. The TiN-reinforced composite showed optimal wear performance with a wear rate of 5.02 × 10^{-8} mm^3 /Nm at a 10 N applied load, which is a considerable improvement compared with the HEA wear rate of 6.17 × 10^{-4} mm^3 /Nm at the same applied load. Along the same line, the synergistic effect of both ceramics was found to be beneficial, resulting in the lowest COF of 0.071 at 20 N applied load for the HEA-VC-TiN

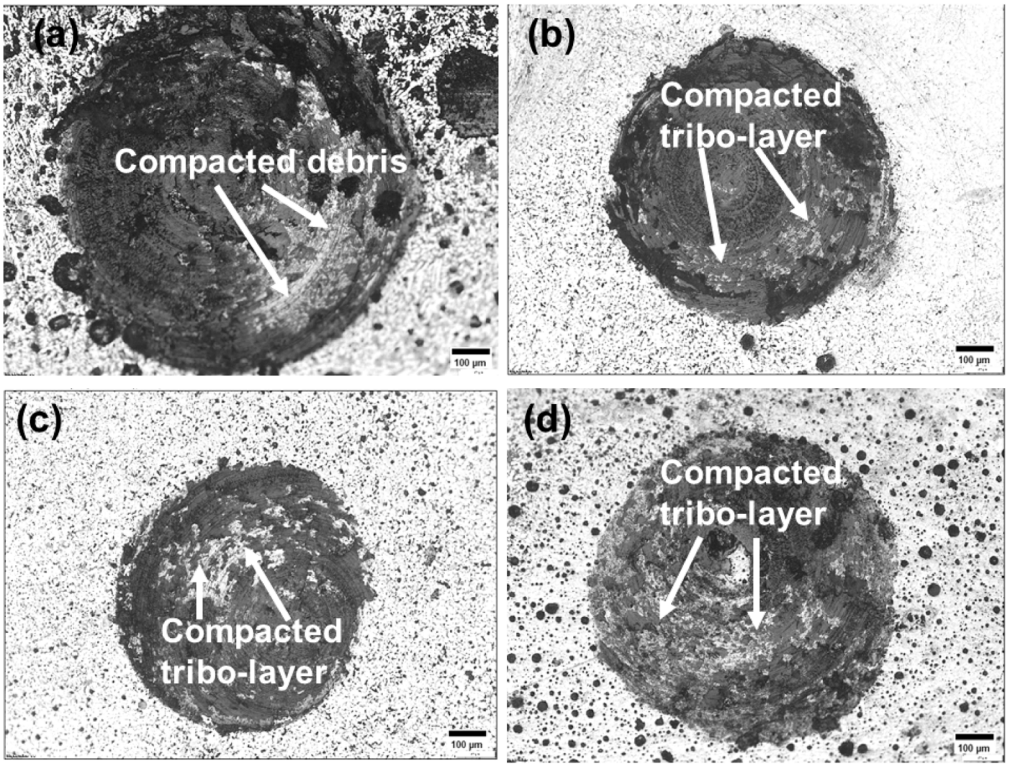

Fig. 11. Micrographs of the worn tracks of (a) HEA (b) HEA-VC (c) HEA-TiN (d) HEA-VC-TiN.

Table 4
Summary of corrosion test data for the HEA and its composites.

Samples	Corrosion Potential Ecorr (V)	Corrosion Current Density jcorr (A/cm^2)	Polarization Resistance (Ω)	Corrosion Rate (mm/year)
HEA	– 0.14618	5.90×10^{-5}	567.79	0.6909
HEA-VC	– 0.05481	1.81×10^{-4}	227.68	2.1051
HEA-TiN	– 0.0819	1.38×10^{-4}	256.98	1.5738
HEA-VC-TiN	– 0.000691	6.27×10^{-5}	472	0.7291

composite. Hence, the samples' COF profiles at 20 N applied load was presented in Fig. 10. The COF behaviour revealed that all curves demonstrated initial run-in stages (0–2500 cycles) and final stabilisation stages (2500–6000 cycles). The fluctuations observed in the initial run-in stages could be attributed to frictional shear tearing between the contacting surfaces [17].

Additionally, an intermittent spike was observed in the COF profile of the HEA-VC composite at approximately 1500 cycles. This spike is attributed to a transient adhesive scuffing regime, followed by a self-healing stabilisation phase. The scuffing phenomenon in the composite arises from the mismatch at the interface between the hard VC reinforcement and the relatively softer HEA matrix [41]. As sliding progresses, strain accumulates at the particle-matrix interface. The spike indicates the moment when this accumulated strain leads to a localised breakdown of the mechanically mixed tribo-debris, resulting in micro-welding between adjacent asperities. The trends observed in the matrix and other composite profiles differ due to the more uniform deformation of the HEA, which lacks the rigid ceramics that might anchor or disrupt the tribo-film. Furthermore, the lower adhesive affinity of TiN for most metallic sliding interfaces contrasts with that of VC.

The micrographs of the worn tracks of the HEA and its composites, subjected to a 20 N applied load, are presented in Fig. 11. In the HEA matrix worn track depicted in Fig. 11a, the metal-to-metal contact resulted in the formation of loose wear debris due to initial abrasive wear, which became trapped within the sliding interface. This debris underwent forced aggregation and cold-welding processes under high-pressure contact forces that induced mechanical stress during repeated sliding. Consequently, this led to the deformation of the softer CoCrNi and Cu-rich phases, which are reinforced by the hard Laves phases, forming a strain-hardened protective tribo-layer that inhibits further deformation of the HEA. This suggests that the matrix possesses the capacity for strain hardening, although it initially exhibits wear from

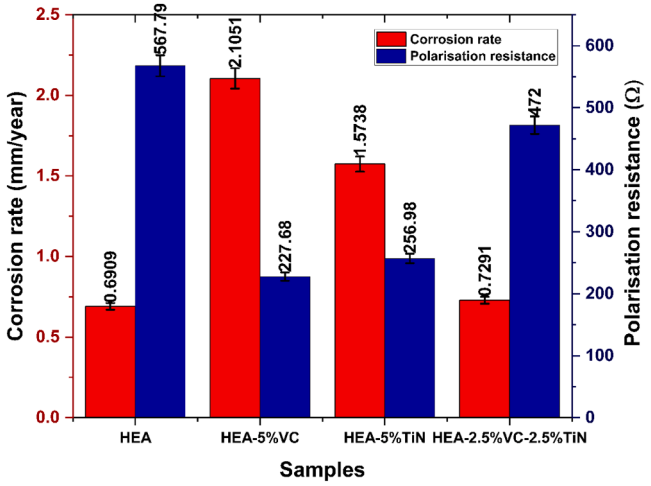

Fig. 13. Corrosion rate and polarisation resistance of the HEA and its composites.

abrasive and adhesive mechanisms.

In Fig. 11 b and c, the VC and TiN particles dispersed within the HEA matrix function as load-bearing sites, limiting the extent of deformation in the softer phases of the matrix. Adding the ceramics makes the surface harder, as shown by the hardness values of the composites. This, in turn, reduces the volume of loose debris and makes deep ploughing less likely than with the HEA matrix alone. The worn track images of the composites also show a denser, more continuous, and uniform tribo-layer. This suggests that the matrix-ceramic combination has improved the tribo-layers that form within the composites. The synergistic effect of incorporating both ceramics into the HEA promotes the development of a stable glaze layer that serves as a protective shield, effectively shifting the wear regime from severe adhesive wear to a milder wear loss and more stable condition [42]. The tribo-layer has reduced the COF from 0.542 for the HEA matrix to 0.154, 0.192, and 0.071 for the VC-, TiN-, and VC-TiN-reinforced composites, respectively.

Corrosion resistance of the HEA and its composites

The corrosion resistances of the HEA and its composites were investigated, and the experimental results are presented in Table 4, Figs. 12 and 13. The corrosion resistances of HEA and its composites

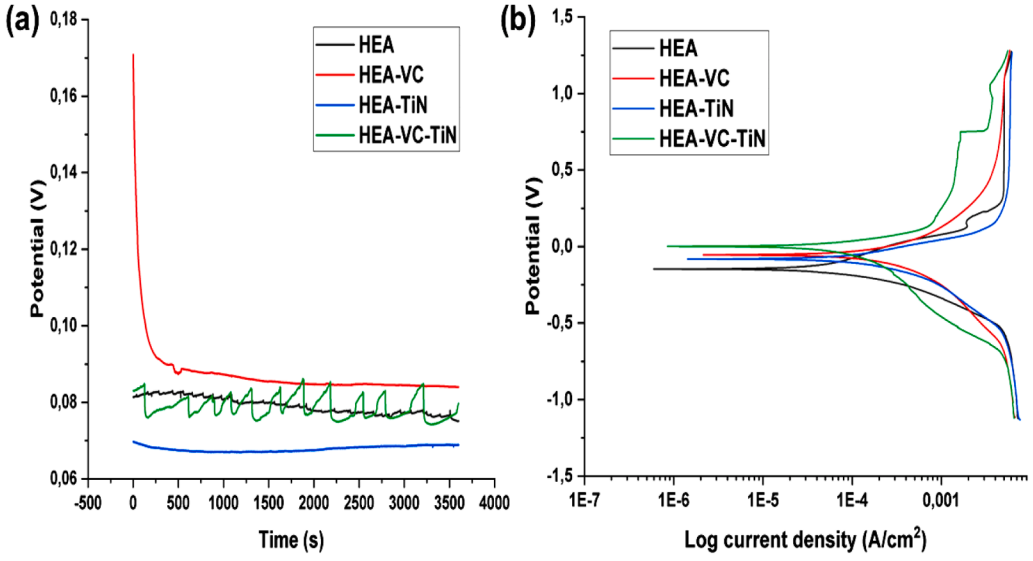

Fig. 12. (a) OCP curves and (b) Potentiodynamic polarisation resistance of the HEA and its composites.

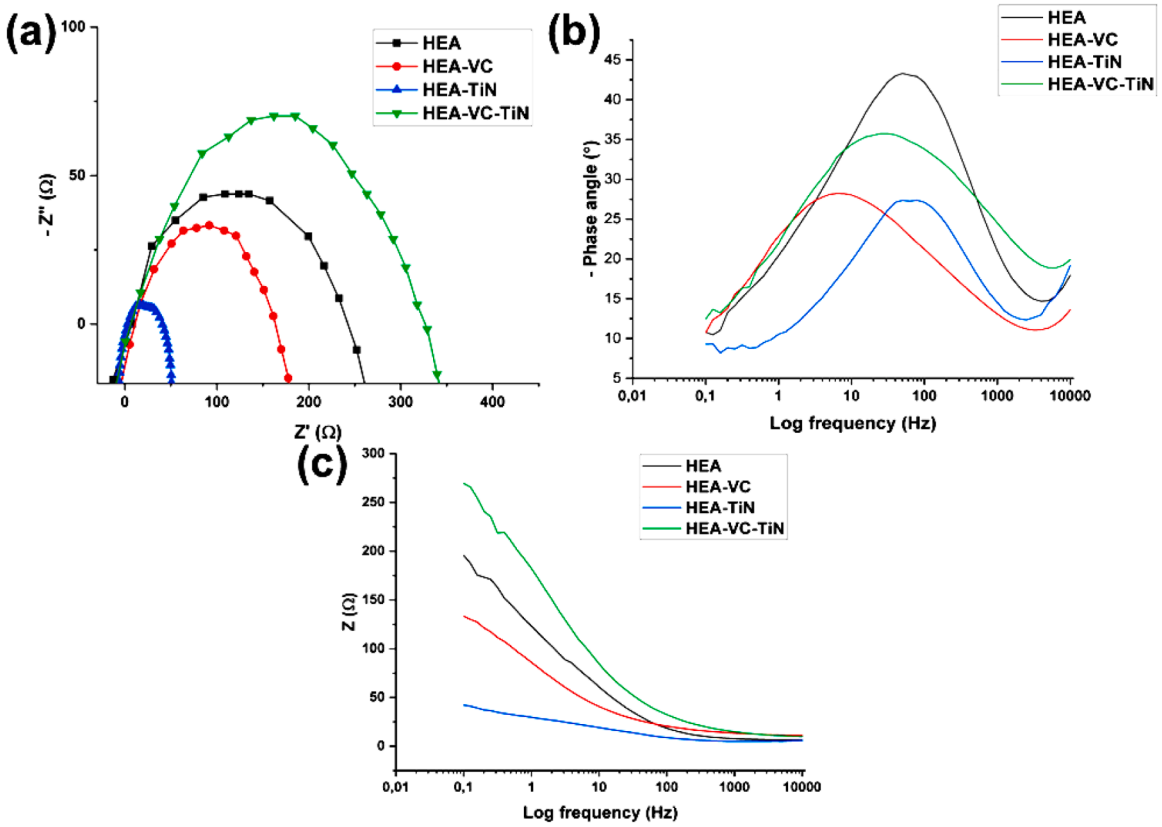

Fig. 14. (a) Nyquist (b) Phase angle (c) Bode Modulus.

were investigated over time in the 0.5 M H_2SO_4 electrolyte via open circuit potential (OCP) measurement. The samples underwent an hour-long OCP test, and at zero applied current, their OCP values were noted.

The open circuit potential changes over time for the samples are illustrated in the OCP curves presented in Fig. 12a. During the OCP measurement period, a slight fluctuation in potential around 0.080 V was observed in the OCP curve of the HEA, while the VC-TiN-reinforced composite exhibited a more pronounced potential oscillation around 0.082 V. This behaviour indicates the breakdown of a localised passive layer, followed by passivation regimes occurring on the surfaces of the samples. The OCP profile for the VC-reinforced HEA began at a more noble potential of approximately 0.17 V but experienced a sharp decline within the first 500 s, stabilising around 0.084 V after the initial drop. The rapid decrease prior to stabilisation suggests the breakdown of the pre-existing surface layer before the composite achieved steady-state equilibrium with the corrosive medium. Throughout the testing period, the TiN-reinforced composite exhibited the lowest and most stable OCP at 0.069 V. The long-term steady state observed is indicative of a stable passive film that protects the bulk metal from rapid degradation [43].

The potentiodynamic polarisation curves depicted in Fig. 12b illustrate that both the HEA and its composites display distinctive active-passive transition regions; however, their passivation behaviour is similar. The HEA demonstrated excellent corrosion resistance, quantified at 0.6909 mm/year, with a corrosion potential of –0.14618 V, a corrosion current of 5.90×10^{-5} A/cm^2, and a polarisation resistance of 567.79 Ω, likely due to the formation of a protective passive film. The synergistic effect of the reinforcements in the HEA-VC-TiN composite resulted in the lowest corrosion current density of 6.27×10^{-5} A/cm^2, indicating good corrosion resistance. However, the composite exhibited a slightly higher corrosion rate of 0.7291 mm/year compared to the HEA, which is unexpected, given that lower current densities are typically associated with higher corrosion resistance. This anomaly may be attributed to the ceramic-metal interfaces introduced by the addition of reinforcements, potentially leading to galvanic coupling that promotes localised corrosion. This finding is supported by the higher corrosion currents of 1.81×10^{-4} and 1.38×10^{-4} A/cm^2 observed in the VC- and TiN-reinforced composites, respectively.

On the other hand, the HEA demonstrated a more negative corrosion potential of –0.14618 and a comparatively lower current density of 5.90×10^{-5} A/cm^2, as shown in Table 4, suggesting it as a better-performing corrosion resistance candidate than the HEA-VC-TiN composite. This is evidenced by its lower corrosion rate of 0.6909 mm/year and higher polarisation resistance of 567.79 Ω, as shown in Fig. 13 and Table 4.

The observations from the potentiodynamic investigation are further corroborated by the Nyquist and phase angle plots in Fig. 14a–c, which revealed that the HEA and HEA-VC-TiN-reinforced composite had the largest arch diameters, which signified their better resistance to charge transfer compared to the other samples.

Furthermore, the highest phase angle exhibited by the HEA confirmed that the well-formed passive film on its surface displayed a double-layer capacitance and acted as a barrier to charge transfer, indicating that the HEA possessed excellent corrosion resistance. The findings align with the research of Tanji et al. [44] and Zhang et al. [16], both of whom agreed that a larger Nyquist plot arch diameter is indicative of superior corrosion resistance in samples. It is important to note that capacitive loops of larger diameters can be ascribed to an increase in passive film resistance, which is associated with better corrosion resistance [45,46]. A higher loop diameter is inversely proportional to a higher resistance to charge transfer and, hence, a lower corrosion rate [47,48].

Finally, some literature data for the hardness value, COF and corrosion current density of 316 L stainless steel are listed in Table 5 for comparison. The hybrid composite in this work exhibited a superior hardness value to the stainless steel and outperformed it tribological

Table 5
Summary of the hardness value, coefficient of friction and corrosion resistance of the HEA-VC-TiN composite.

Material	Hardness value (HV)	Coefficient of Friction (μ)	Corrosion current density (A/cm^2)	Ref.
This hybrid	736 ± 30.79	0.071	6.27×10^{-5}	-
316 L Stainless Steel	230 ± 7	0.647	1.18×10^{-5}	[12]

performance. The hybrid also compares favourably with the steel's corrosion resistance in 0.5 M sulphuric acid.

Conclusion

In this study, high-entropy alloys (HEA) were successfully fabricated using directed energy deposition, along with vanadium carbide (VC), titanium nitride (TiN), and a combination of both ceramics. These materials were characterised for their potential applications in surface engineering, specifically in cladding and laser surface alloying. The results led to the following conclusions.

1. The developed HEA resulted in the formation of multiple phases, significantly influencing its structure-property characteristics. The reinforcement of the HEA with ceramics, in both separate and combined proportions, facilitated further enhancements in its properties. The modifications could markedly affect its performance in specific surface engineering applications, particularly in terms of improving wear and corrosion resistance in harsh environments.
2. Significant enhancements in hardness values and tribological properties were observed when reinforcing the HEA with various ceramics. The composite exhibited a more than twofold increase in hardness, rising from 196 ± 8.55 HV to 443 ± 69.64 HV with VC reinforcement. The TiN- and VC-TiN-reinforced composites demonstrated nearly a fourfold improvement in hardness values, achieving 721 ± 22.28 HV and 736 ± 30.79 HV, respectively. The TiN-reinforced composite also displayed optimal wear resistance, reducing the wear rate of the HEA from approximately $\times 10^{-4}$ to $\times 10^{-6}$ mm^3 /Nm under a 20 N applied load. However, the synergistic effect of both ceramics led to a lower and more stable COF of 0.071, which represents a substantial reduction compared to the 0.542 and 0.192 COFs observed for the HEA and its TiN-reinforced composite, respectively, at the same load.
3. The corrosion test revealed that the HEA exhibited the highest polarisation resistance at 567.79 Ω, alongside a corrosion rate of 0.6909 mm/year. This was closely followed by the combined ceramic-reinforced composite, which demonstrated a polarisation resistance of 472 Ω and a corrosion rate of 0.7291 mm/year. These results indicate that reinforcing the HEA with both ceramics provides superior corrosion resistance compared to the individual ceramic-reinforced composites.

Finally, the properties of $Co_{22.2}Cr_{22.2}Ni_{22.2}Cu_{22.2}Nb_{11.2}$ HEA were successfully improved for surface engineering applications by reinforcing it with different ceramics. The experimental results indicated that the composites are suitable for surface engineering processes, including cladding for surface protection against corrosion and wear, as well as surface alloying for refurbishing worn surfaces.

CRediT authorship contribution statement

Ayo Samuel Alabi: Writing – original draft. **Abimbola Patricia Idowu Popoola:** Writing – review & editing, Supervision. **Olawale Mohammed Popoola:** Supervision, Data curation. **Mathe Ntombizodwa Ruth:** Writing – review & editing, Supervision.

Declaration of Competing Interest

The authors declare that they have no known competing financial interests or personal relationships that could have appeared to influence the work reported in this paper.

Acknowledgements

The authors acknowledge the supports of the Surface Engineering Research Laboratory, Tshwane University of Technology, Pretoria, South Africa and The Photonic Centre, Council for Scientific and Industrial Research, Pretoria, South Africa.

References

[1] Z. Wu, H. Bei, F. Otto, G.M. Pharr, E.P. George, Recovery, recrystallization, grain growth and phase stability of a family of FCC-structured multi-component equiatomic solid solution alloys, Intermetallics 46 (2014) 131–140.
[2] D. Xu, M. Wang, T. Li, X. Wei, Y. Lu, A critical review of the mechanical properties of CoCrNi-based medium-entropy alloys (pp. N/A-N/A), Microstructures 2 (1) (2022) (pp. N/A-N/A).
[3] H. Cheng, et al., The influence of L12 ordered precipitates on hydrogen embrittlement behavior in CoCrNi-based medium entropy alloys, Acta Mater. 260 (2023) 119328.
[4] H. He, Y. Wang, Y. Qi, Z. Xu, Y. Li, Review on the preparation methods and strengthening mechanisms of medium-entropy alloys with CoCrNi as the main focus, J. Mater. Res. Technol. 27 (2023) 6275–6307.
[5] H. Wang, et al., Multifunctional high entropy alloys enabled by severe lattice distortion, Adv. Mater. 36 (17) (2024) 2305453.
[6] M. Mozetič, et al., Recent developments in surface science and engineering, thin films, nanoscience, biomaterials, plasma science, and vacuum technology, Thin Solid Films 660 (2018) 120–160.
[7] I. Moravcik, et al., Interstitial doping enhances the strength-ductility synergy in a CoCrNi medium entropy alloy, Mater. Sci. Eng. A 781 (2020) 139242.
[8] D.E. Jodi, N. Park, Phase separation and its effect on atomic interactions in CoCrNiCux medium-entropy alloys, Mater. Lett. 255 (2019) 126528.
[9] Y. Ren, et al., A wear-resistant metastable CoCrNiCu high-entropy alloy with modulated surface and subsurface structures, Friction 10 (10) (2022) 1722–1738.
[10] W. Lu, X. Luo, Y. Yang, B. Huang, Effects of Nb additions on structure and mechanical properties evolution of CoCrNi medium-entropy alloy, Mater. Express 9 (4) (2019) 291–298.
[11] X. Ding, et al., Effect of Al addition on microstructure and properties of CoCrNi medium-entropy alloy prepared by powder metallurgy, Materials 15 (24) (2022) 9090.
[12] H. Wu, S. Zhang, C. Wu, C. Zhang, X. Sun, X. Bai, Electrochemical corrosion behavior in sulfuric acid solution and dry sliding friction and wear properties of laser-cladded CoCrFeNiNbx high entropy alloy coatings, Surf. Coat. Technol. 460 (2023) 129425.
[13] S. Riva, A. Tudball, S. Mehraban, N.P. Lavery, S.G. Brown, K.V. Yusenko, A novel High-Entropy Alloy-based composite material, J. Alloy. Compd. 730 (2018) 544–551.
[14] Y. Hu, et al., Cf/(CrZrHfNbTa) C–SiC high-entropy ceramic matrix composites for potential multi-functional applications, J. Mater. Sci. Technol. 182 (2024) 132–140.
[15] M.T. Parizi, G. Ebrahimi, H. Ezatpour, M. Gupta, J. Li, W. Guo, Trimodal hierarchical structure in the carbonaceous hybrid (GNPs+ CNTs) reinforced CoCrFeMnNi high entropy alloy to promote strength-ductility synergy, Mater. Sci. Eng. A 850 (2022) 143446.
[16] J.-d Zhang, L. Zhang, H.-z Ma, In-situ development of Ti (C, N) and their effect on microstructure, wear and corrosion properties of CoCrFeNiTi high-entropy alloy matrix composites, Vacuum 221 (2024) 112914.
[17] J. Han, et al., Microstructure and wear property of (TiN+ NbC) double ceramic phase-reinforced in FeCrNiCoAl high-entropy alloy coating fabricated by laser cladding, Ceram. Int. 50 (23) (2024) 49066–49084.
[18] X. Wang, S. Zhang, F. Zhao, Z. Wu, Z. Xie, Structural evolution and fracture mechanism of WC-Particle-Reinforced FeCoCrNiMn High-Entropy Alloy Coatings, Coatings 14 (4) (2024) 403.
[19] G. Liang, G. Jin, X. Cui, Z. Qiu, J. Wang, Investigation on the relationship between reinforcing behavior of TiN and wear resistance of AlCoCrCuNiTi high-entropy alloy coating, Appl. Surf. Sci. 593 (2022) 153419.
[20] K. Yu, W. Zhao, Z. Li, N. Guo, G. Xiao, H. Zhang, High-temperature oxidation behavior and corrosion resistance of in-situ TiC and Mo reinforced AlCoCrFeNi-based high entropy alloy coatings by laser cladding, Ceram. Int. 49 (6) (2023) 10151–10164.
[21] K.N. Braszczyńska-Malik, Types of component interfaces in metal matrix composites on the example of magnesium matrix composites, Materials 14 (18) (2021) 5182.
[22] S. Ragunath, N. Radhika, B. Saleh, Advancements and future prospects of additive manufacturing in high-entropy alloy applications, J. Alloy. Compd. 997 (2024) 174859.

[23] X.-Z. Wang, Q. Hu, L. Zhang, Z. Cui, The influence of Nb addition on the passivity of CoCrNiNbx multi-principal element alloys, J. Electroanal. Chem. 908 (2022) 116107.
[24] J. Hong, S. Li, L. Zhang, J. Yang, Effect of Nb content on the microstructure and mechanical properties of CoCrNiNbx high-entropy alloy, in: Journal of Physics: Conference Series, 2760, IOP Publishing, 2024 012010.
[25] Z. Pan, et al., Segregation of solute elements and strengthening effects of CoCrNiCux medium-entropy alloys: a combined experimental and simulation study, J. Alloy. Compd. 941 (2023) 169015.
[26] Y. Cai, Y. Chen, Z. Luo, F. Gao, L. Li, Manufacturing of FeCoCrNiCux medium-entropy alloy coating using laser cladding technology, Mater. & Des. 133 (2017) 91–108.
[27] S. Hosseini, M.S. Khorrami, M.H. Sohi, In-situ composite formation of vanadium carbide in CrFeCoNiCu high-entropy alloy cladded on AISI304 stainless steel, J. Mater. Res. Technol. 35 (2025) 3333–3340.
[28] Y. Xie, Z. Xia, J. Hou, J. Xu, P. Chen, L. Wan, Effect of Cu-Rich Phase Precipitation on the Microstructure and Mechanical Properties of CoCrNiCu x Medium-Entropy Alloys Prepared via Laser Directed Energy Deposition, Acta Metall. Sin. (Engl. Lett.) 34 (11) (2021) 1591–1600.
[29] L. Zhang, H. Zhang, H. Cao, X. Chen, Y. Fang, G. Zheng, Enhanced tribocorrosion performance of laser-deposited Fe2CoNiCrAlTiCx high-entropy alloy coatings via in-situ graphitization in aqueous medium, Corros. Sci. 236 (2024) 112221.
[30] H. Chen, et al., Hierarchical microstructures and strengthening mechanisms of nano-TiC reinforced CoCrFeMnNi high-entropy alloy composites prepared by laser powder bed fusion, J. Mater. Sci. Technol. 136 (2023) 245–259.
[31] B. Li, L. Zhang, B. Yang, Grain refinement and localized amorphization of additively manufactured high-entropy alloy matrix composites reinforced by nano ceramic particles via selective-laser-melting/remelting, Compos. Commun. 19 (2020) 56–60.
[32] B. Jin, N. Zhang, S. Yin, Strengthening behavior of AlCoCrFeNi (TiN) x high-entropy alloy coatings fabricated by plasma spraying and laser remelting, J. Mater. Sci. Technol. 121 (2022) 163–173.
[33] K. Ma, L. Feng, J. Liu, Y. Zhao, Controllable preparation of carbide-containing FeCr2MnAlCu high-entropy alloys: microstructure and mechanical properties, J. Alloy. Compd. (2026) 186285.
[34] Y. Chen, Q. Zhou, Directed energy deposition additive manufacturing of CoCrFeMnNi high-entropy alloy towards densification, grain structure control and improved tensile properties, Mater. Sci. Eng. A 860 (2022) 144272.
[35] W. Wang, et al., Microstructural Evolution and Strengthening Mechanisms of SiC-Reinforced FeCoNiCrAl Coatings by Laser Directed Energy Deposition, Int. J. Precis. Eng. Manuf. (2026) 1–36.
[36] Y. Wang, L. Zhao, D. Wan, S. Guan, K. Chan, Additive manufacturing of TiB2-containing CoCrFeMnNi high-entropy alloy matrix composites with high density and enhanced mechanical properties, Mater. Sci. Eng. A 825 (2021) 141871.
[37] G.-D. Chen, et al., Strengthening mechanisms of laser cladding TiC/FeCoCrNiCu high-entropy composite coatings: Microstructure evolution and wear behaviors, Tribology Int. 199 (2024) 109979.
[38] B.C. Delaney, Q.J. Wang, V. Aggarwal, W. Chen, R.D. Evans, A contemporary review and data-driven evaluation of Archard-type wear laws, Appl. Mech. Rev. 77 (2) (2025) 022101.
[39] R. Casati, State of the Art of Metal Matrix Nanocomposites, Alum. Matrix Compos. Reinf. Alumina Nanopart. (2015) 1–35.
[40] S. Ragunath, N. Radhika, S.A. Krishna, A. Pramanik, Microstructural, electrochemical, and hot corrosion analysis of CoCrFeCuTi high entropy alloy reinforced titanium matrix composites synthesized by microwave sintering, Int. J. Lightweight Mater. Manuf. 8 (1) (2025) 141–155.
[41] B. Podgornik, Adhesive wear failures, J. Fail. Anal. Prev. 22 (1) (2022) 113–138.
[42] C. Zhang, R.W. Neu, Understanding the role of glaze layer with aligned images from multiple surface characterization techniques, Wear 477 (2021) 203837.
[43] A. Wetzel, et al., Long-term corrosion studies of CrCoNi and CrMnFeCoNi in sulfuric acid, npj Mater. Degrad. 9 (1) (2025) 86.
[44] A. Tanji, R. Feng, Z. Lyu, R. Sakidja, P.K. Liaw, H. Hermawan, Passivity of AlCrFeMnTi and AlCrFeCoNi high–entropy alloys in Hanks' solution, Corros. Sci. 210 (2023) 110828.
[45] J. Zhu, et al., Microstructures, wear resistance and corrosion resistance of CoCrFeNi high entropy alloys coating on AZ91 Mg alloy prepared by cold spray, J. Alloy. Compd. 925 (2022) 166698.
[46] C. Zhang, L. Huang, S. Li, K. Li, S. Lu, J. Li, Improved corrosion resistance of laser melting deposited CoCrFeNi-series high-entropy alloys by Al addition, Corros. Sci. 225 (2023) 111599.
[47] M. Dehestani, S. Sharafi, G.R. Khayati, Electrodeposited FeCoNiWMo high entropy alloy/SiC nanocomposite coatings: Microstructure, mechanical properties and corrosion resistance, Intermetallics 162 (2023) 107988.
[48] D. Jiang, H. Cui, H. Chen, X. Zhao, G. Ma, X. Song, Wear and corrosion properties of B4C-added CoCrNiMo high-entropy alloy coatings with in-situ coherent ceramic, Mater. & Des. 210 (2021) 110068.